ELSEVIER

Contents lists available at ScienceDirect

Materials & Design

journal homepage: www.elsevier.com/locate/matdes



Ripple formations determine the heterogeneous microstructure of directed energy deposition (DED)-printed 316L components



Himanshu Balhara, Bhaskar Botcha, Sarah J. Wolff, Satish T.S. Bukkapatnam*

Wm Michael Barnes'64 Department of Industrial and Systems Engineering, Texas A&M University, College Station, TX 77840, United States

HIGHLIGHTS

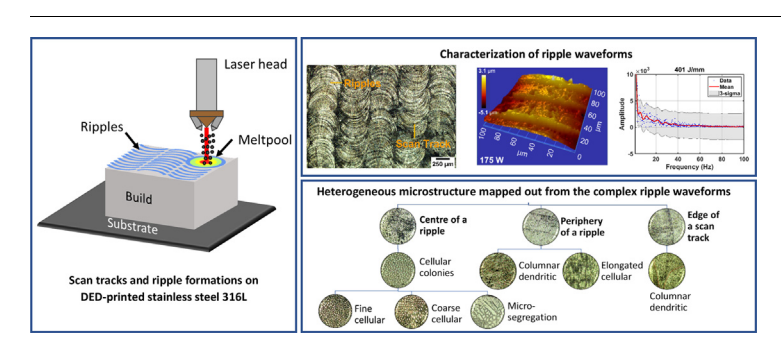
- Reports the effect of laser directed energy deposition (DED) parameters on the multi-scale microstructure, as well as the nature and the characteristics of the morphological formations on surface, namely, ripple waveforms and scan tracks.
- Establishes that the heterogeneities in the type, size and orientations of the microstructure and dendritic patterns on scan surface of DED-printed 316L components are informed by the ripple patterns.
- The complex waveform patterns of the ripples and their variations with laser power indicate that additional phenomena beyond the Marangoni effect determine the mass transport in the melt pool regions in a DED process.

ARTICLE INFO

Article history: Received 11 November 2022 Revised 6 February 2023 Accepted 14 February 2023 Available online 18 February 2023

Keywords: Directed Energy Deposition (DED) Ripples Microstructure 316L

G R A P H I C A L A B S T R A C T



ABSTRACT

This paper presents an experimental study to characterize the ripples and other morphological formations as well as their influence on the heterogeneous microstructure on the surfaces of the directed energy deposition (DED)-printed stainless steel (316L) components. While ripple formations in the welding literature have been studied extensively, they have not received much attention in the DED process. They are often wrongly conflated with the melt pool geometry. The experiments consisted of printing 10 mm cubic components on a hybrid machine tool (MTS 500 from Optomec) under nine different combinations of laser power, scan speed and dwell time. The ripple formations and the microstructure on the scan surface were subsequently observed and statistically characterized at four different magnifications on an optical microscope. The study establishes that the ripple traces are a main determinant of the dendritic structures, as well as the heterogeneous spatial distribution of the microstructure formations in DED-printed 316 components. The statistical characterization also highlights the limitations of the ripple waveform descriptors employed commonly in the welding literature and introduces spectral quantifiers to adequately capture the complex waveform patterns of ripples in DED.

© 2023 The Authors. Published by Elsevier Ltd. This is an open access article under the CC BY license (http://creativecommons.org/licenses/by/4.0/).

E-mail address: satish@tamu.edu (S.T.S. Bukkapatnam).

^{*} Corresponding author.

1. Introduction

The powder-fed or blown-powder Directed Energy Deposition (DED) is increasingly considered in the industry for additive manufacturing (AM) of near-net-shape metallic components. The market for DED is growing at an annual rate of 15% and would reach \$600 M by 2026 [1]. In particular, this process considered for printing advanced functional alloy, high-precision components in the bio-implant and aerospace industry [2], refurbishing industrial components, such as turbine blades, nuclear reactor parts, and hard-facing different substrate materials [3]. The DED process employs a laser beam (see Fig. 1a) to melt the powders as they emerge from the nozzles, and impinge into a melt pool [4]. Compared to many AM processes, DED offers higher material deposition rate and a better spatial compositional control.

More pertinently, the process parameters such as laser power, scan speed, dwell time, and powder flow rate have a significant bearing on thermal and mass-flow fields in DED [5]. Unlike other AM processes, both the thermal and mass-flow fields affect the morphological formations, particularly the scan track and ripple patterns on the surface (Fig. 1b), and these morphological patterns in effect are the key determinants of the spatial distribution of microstructure. As evidenced in the present work, in DED-printed stainless-steel AISI 316L, microstructure patterns are highly heterogeneous and are spread over multiple length scales, extending from a few 100 nm up to 1 mm [6].

While the occurrence of many of these microstructure patterns have reported in DED, characterization of the spatial distribution of ripples and these microstructures under different process parameters has not been addressed to date. In fact, over 50 studies have reported the microstructural patterns occurring in the DED-printed 316L components (see supplementary section [25–33,36–39,41–46,48,50,51]). A vast majority of these studies have focused on capturing the microstructural patterns in the so-called build direction, i.e., across multiple layers of material deposition under different process conditions (see supplementary section). Only five studies have discussed the microstructural patterns in the scan direction (i.e., within a single layer and over a scan plane) (see [34,35,40,47,49]).

Surprisingly, the ripple formations (see Fig. 1b, Fig. 2(a&b)) and their influence on the diverse microstructure patterns are mostly overlooked in the DED literature. At times, ripples are wrongly conflated with the meltpool geometric features [7]. As shown in Fig. 1 (a,b), ripples are essentially surface waves that form along the scan tracks or X-Y plane. The schematic in Fig. 1a illustrates that ripples propagate in the scan direction. The micrograph in Fig. 1b depicts successive scan tracks containing the traces of multiple ripples. It

may be noted that the mechanism of ripple formation has been studied extensively in the welding literature (e.g., [8–10]), and to an extent for the selective laser melting (SLM) process [11–13] but not for DED. This gap is further underscored by the evidence from the present experimental study that the morphological formations, particularly, the ripples and track marks inform the heterogeneous microstructure clusters spread over different scales. In fact, much of the heterogenous microstructure of DED-printed 316L components can be predicted based on the ripple formations.

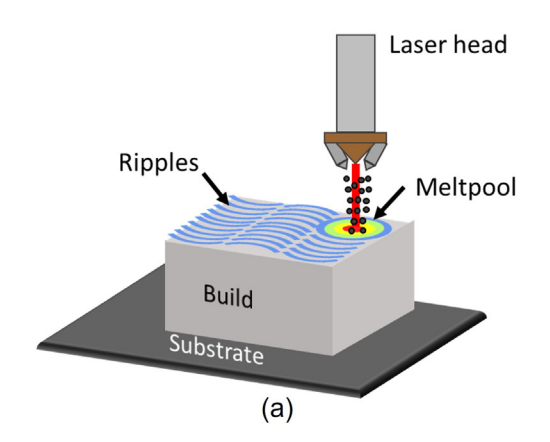
This work is the perhaps first experimental and micrographical image analysis study towards direct observation and statistical quantification of these formations, and the delineation of how the DED process parameters, especially the laser power influence ripple formations (Fig. 1b), and how the ripple formations, in turn determine the heterogenous spatial distribution of the microstructure. These microstructure patterns, including the grain type, size, orientation, and distribution over multiple scales wield a significant, at times, deleterious influence on the mechanical properties and functionality of the DED-printed 316L components.

The experimental studies reported in the sequel also suggest that the ripples in DED are complex waves of varying amplitude and frequencies. For example, a representative heightmap of the surface of a DED-printed component obtained using white light interferometry (Fig. 2a, b) captures variations in amplitudes and wavelengths (both of order of 10 μm). The observations from the micrograph study reported in the sequel suggest that the quantifiers, such as average amplitude and average pitch employed in the literature to quantify the ripple pattern would be inadequate to capture the complex waveform patterns of ripples in DED. We adapt techniques from the spectral and image analysis literature to develop suitable statistical quantifiers of the ripple formations.

In summary, the main contributions of this paper are two-fold:

(1) This study establishes how the morphological formations, especially the ripples and scan tracks are the chief determinants of the heterogeneous microstructure and its distribution on the scan face/surface of a 316L part printed using a DED process. The study also delineates the influence of the process parameters, namely the laser power, the scan speed and the dwell time on the morphological formations and the microstructure. This is perhaps the first study to characterize morphological features and the spatial distribution of heterogenous microstructure as informed by the ripples in a DED process.

(2) This study provides a quantitative assessment of the variation of the geometry of the ripple formations with process parameters employing statistical and image analysis methods and relates these experimental results to the prior understandings of ripple formations reported in the welding literature. The study also



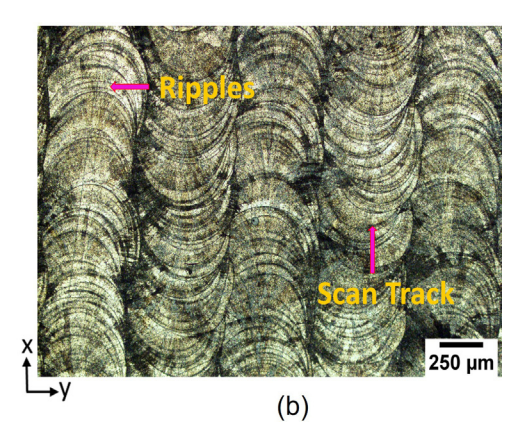


Fig. 1. (a) Schematic of a powder-fed or blown-powder DED process; (b) a representative optical micrograph showing the scan tracks and ripple formations on DED-printed 316L parts.

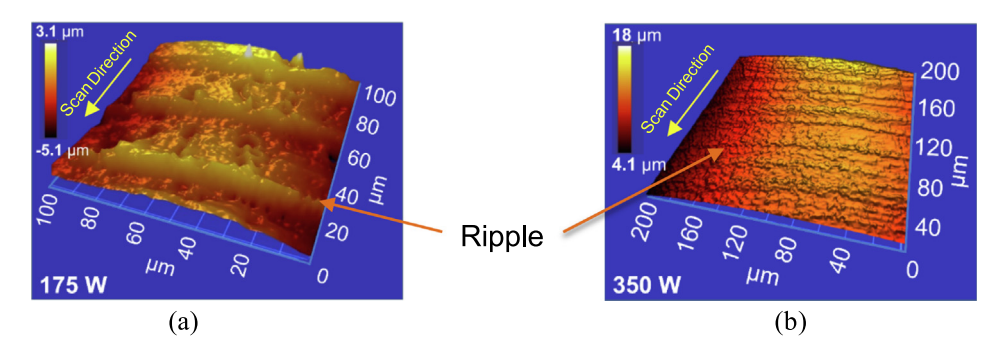


Fig. 2. (a,b) Representative ripples formations on the as-printed surface of 316L gathered using white light interferometry instrument showing recurring waveforms containing multiple wavelengths and amplitude variations. Such ripple waveforms as well as their effect on the microstructure have not been studied in the literature.

shows the extent to which the analytical models adapted from the welding process literature can capture the variation of the ripple widths and their wavelengths with process.

The remainder of this paper is organized as follows. Section 2 describes the experimental study to accumulate the various microstructure images; the multi-scale microstructure patterns of the DED-printed 316L samples from these experiments are presented in Section 3. Section 4 discusses the heterogeneity of the dendritic structure and the effect of process parameters on ripple geometry; concluding remarks are summarized in Section 5. Additionally, a supplementary section presenting a concise literature review of the microstructure studies on DED-printed 316L samples is appended.

2. Experimental approach

2.1. Experimental setup

The experiments consisted of printing stainless steel 316L samples of dimensions 10mm × 10mm × 10mm using an Optomec-LENS® MTS 500 at Texas A&M University [52]. The machine tool is essentially a 4-axis CNC machine that automatically controls the worktable motion in X and Y directions, motion of the laser and a milling head along a Z (vertical) axis, and the rotation of a horizontal spindle, which can be used to clad and repair a variety of freeform parts. This machine tool uses a continuous IPG YLR-1000 fiber laser with a spot size of 600 µm and a wavelength of 1070 nm. It also comprises two powder feeder hoppers with an option to extend to four hoppers. The powder from individual hoppers is transported to a mixing chamber and finally delivered through four nozzles using pressurized argon. Besides powder transport and delivery, argon also helps to reduce oxidation during deposition and serves as a shielding gas during deposition. The machine tool is capable of maintaining oxygen levels in the chamber to <40 ppm. For the current set of experiments, an open atmosphere (OA) mode was used. The schematic and working principles of DED are illustrated in Section 1, Fig. 1(a). A highly focused laser beam interacts with the powder particles and forms a melt pool which eventually solidifies along the direction of the scan. The machine, through a Siemens 828D controller, provides control over multiple process parameters such as powder composition, powder feed rate, laser power, hatch spacing, scan speed, and dwell time during the process.

2.2. Experimental design

As noted in Section 2, laser power, scan speed, and dwell time are known to significantly affect the cooling and heating rates, and thereby the scan tracks and ripple formations. Also, as elaborated in Section 4, these process parameters and the formations

have a significant bearing on the microstructures in the part. We therefore focused on how these formations and microstructures of DED-printed 316L at different scales vary with these process parameters.

The settings of these three process parameters were chosen according to an orthogonal Latin hypercube experimental design [14]. This experimental design helps to achieve a maximal spacefilling exploration of the parameter space spanned by laserpower, scan speed, and dwell-time. We also considered the limits (mostly the upper bounds) on the process parameter combinations at which we can operate the machine safely. For example, the maximum laser power should not exceed 600 W, as higher laser power settings tend to create fumes within the OA operating environment. The maximum scan speed was set to 8.46 mm/sec to ensure proper melting. The maximum dwell time was set to 40 s, beyond which the part cools down significantly between successive scans, causing surface distortions [15] that disturb the focusing distance of the laser. Within the set bounds of the process parameters, nine experimental points, as summarized in Table 1 were selected, i.e., one (cubic) sample was printed under each of the nine conditions.

2.3. Experimentation and sample preparation procedures

AISI Stainless Steel 316L with powder particles ranging between 44 and 106μ m in diameter was used in this study. Pertinently, 316L is one of the most popular grades of stainless-steel owing to its exceptional combination of strength and corrosion resistance properties, and is widely used in many engineering domains, including nuclear, aerospace, and automotive sectors. The elemental composition of the powder is mentioned in Table 2. The DED process involved printing nine cubic 316L samples, at process parameter settings stated in Table 1, onto a rectangular 316L substrate of dimensions 76 mm \times 76 mm that has an identical chemical composition as the powders. All samples were printed under the same environmental condition and with the same powder feed rate (feeder RPM: 5 RPM). After the deposition, the top surface of printed parts was machined (end-milled) as-printed, i.e., the substrate surface on which all the samples were built served as a datum and the machined surface was therefore flat within the machine precision relative to the scan direction. As an exception, however, the top surface of as-printed sample 4 was not parallel to the scanning plane due to the excessive heating at high laser power which creates scan tracks with uneven widths and thickness. Consequently, post-milling, the resulting micrographs capture the morphological and microstructural features of multiple layers along the scan direction.

Subsequent to machining, the samples were detached from the substrate using a bandsaw and prepared for microstructure analysis. All the samples were mounted in an epoxy resin with the top surface exposed for polishing. The samples were polished accord-

Table 1DED process parameters settings used to print the nine samples for micrographic studies.

Experiment	Laser power (W)	Scan speed (mm/sec)	Dwell time (sec)	Linear Energy Density (J/mm)
1	487.5	6.56	35	74.31
2	525	3.70	0	141.9
3	562.5	8.46	15	66.48
4	600	1.80	30	333.33
5	450	4.65	20	96.77
6	412.5	2.75	5	150
7	375	5.60	40	66.96
8	337	0.84	25	401.19
9	300	7.40	10	40.54

Table 2 Chemical composition of SS316L powder.

Element	Cr	Ni	Mo	Mn	Cu	P	Si	С	S	Fe
Wt.%	18	13	2.5	2.0	0.5	0.025	0.75	0.03	0.01	Bal.

ing to the usually metallurgical sample preparation for microstructure study. The polishing was performed on a Buehler Automet 250 polisher in multiple steps. The initial steps were conducted at 100 rpm, using 800, 1000, and 1200 grade emery pads, respectively, and the final finish polishing was conducted at 50 rpm using a micro-cloth and colloidal silica. The polished surfaces were etched for 90 s in an Aqua Regia etchant (which contains 3:1 part of HCL and HNO₃). The morphology and the microstructure were observed on the Olympus BX 51 microscope at four different magnifications – 5x (500 μ m length scale), 10x (200 μ m length scale), 20x (100 μ m length scale), and 50x (50 μ m length scale).

3. Results from optical micrography studies

A vast majority of earlier micrography studies of DED-printed 316L had focused on the build direction (see supplementary section). A very few discussed the microstructural patterns along the laser scan direction. Studying the micrographs along the scan direction can contribute to the understanding of the solidification process, the surface morphology, microstructure, and certain defects [15].

Also, as noted earlier, the present study examines the microstructure patterns from the optical micrographs (OMs) taken at four different magnifications. Since the same powder feed rate was employed for all the samples, the deposition rate depends only on the scan speed and the melting process. The study captures the effect of the laser power and scan speed on the ripple formation, as well as scan track marks and void formations in the scan direction, and how they inform the heterogeneity of the microstructure.

Observations at 500 \mu m Fig. 3 shows the representative micrographs which were obtained at 5x magnification, i.e., the microstructures over a field of view of 5.3 mm (500 μm length scale). Fig. 3(a) was obtained from sample 4 that was printed at 600 W laser power and 1.80 mm/sec scan speed. Fig. 3(b) was obtained from sample 5 that was printed at 450 W laser power, and 4.65 mm/sec Fig. 3(c) was obtained from sample 9 that was printed at 300 W laser power and 7.40 mm/sec scan speed.

It may be noted that it is hard to observe the detailed microstructure at such low magnification. However, the large fields of view at this scale allow us to capture the patterns of the scan track [16] as well as the ripples. All three micrographs in the figure show the scan track marks consisting of ripple formations (circular arcs with different color shades) on the trailing edge of the laser head along the scan direction [17]. The various shades present in micrographs are due to the differential action (selectivity) of the

etchant on various chemical compositions and molecular structures present at the sample surface [18].

We further measured the physical overlap and the ripple curvature along the scan direction. We observe that the curvature was uniform across the periphery of every ripple. The ripple curvature (for our case ripple radius) was calculated using a 3-point arc estimate (a utility available in AutoCAD). The average ripple radius was estimated for five ripples on each scan track and their distribution, and the average statistics are presented. As evident in Fig. 4 (a&b), the dimensions of the scan track majorly depend on the laser power and to an extent on the scan speed. The ripple radius appears to increase almost linearly with the laser power. It is worth noting that a significant drift in the center of ripples was observed along multiple scan tracks, especially in the ripples adjacent to the voids.

The extent of the physical overlap between successive scan tracks at various laser power settings can be used to explain the void formations. Here, the overlap is calculated as the ratio of the difference between ripple diameter and the hatch distance, and the ripple diameter. The overlap values at different process settings are summarized in Table 3. The overlap was found to be 60% for sample 4 (600 W, 1.8 mm/s) and −1.53% for sample 9 (300 W, 7.4 mm/s). A negative overlap implies an incomplete fusion between consecutive scan tracks followed by the lack of sufficient material to compensate for the shrinkage, leading to the creation of voids between scan tracks. Due to the temperature-dependent recoil pressure, liquid metal disperses to the edge of melt pool at high laser power, causing the ripple diameter to expand and ultimately increasing the overlap to 60%. In contrast, at low laser power levels, the temperature under the beam decreases, reducing the recoil pressure, consequently the amount of liquid dispersed to the edge of melt pool. This creates small diameter ripples and results in a negative overlap between scan tracks and thus forming voids...

Also, a scan track experiences complicated thermal cycles near the track boundaries—this includes altering the heat transfer patterns due to the effect of the temperatures of the previously laid adjacent tracks, and remelting of solidified tracks at the boundaries with subsequently laid tracks. This introduces interesting morphological formations such as voids as seen in Fig. 3(c) and determines the dendritic structure observed at higher magnifications. Ripples with wavelength < 0.508 mm (as in sample 9 shown in Fig. 3(c) emerge under high scan speed and low laser power. The ripple wavelength increases to 1.812 mm when scan speed is reduced at high laser power settings (as in sample 5).

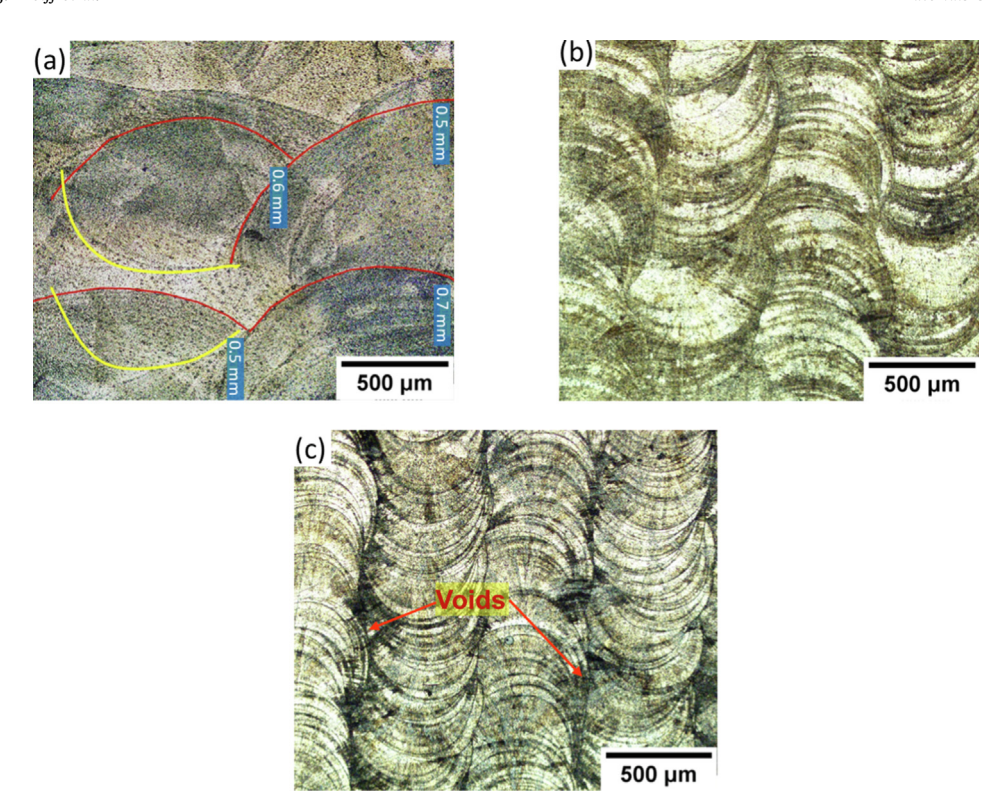


Fig. 3. Optical micrographs at 500 μm scale at three laser power settings: (a) 600 W showing ripples of radius ~ 660 μm with large variations (standard deviation of 230 μm), and highly overlapping scan tracks due to the presence of large shallow melt pool at high laser power; (b) 450 W showing ripples of more uniform radii ~ 307 µm with an overlap of 14 %; (c) 300 W showing ripples of radius \sim 260 μ m with an overlap of -1.53%, that causes void formation between consecutive scan tracks.

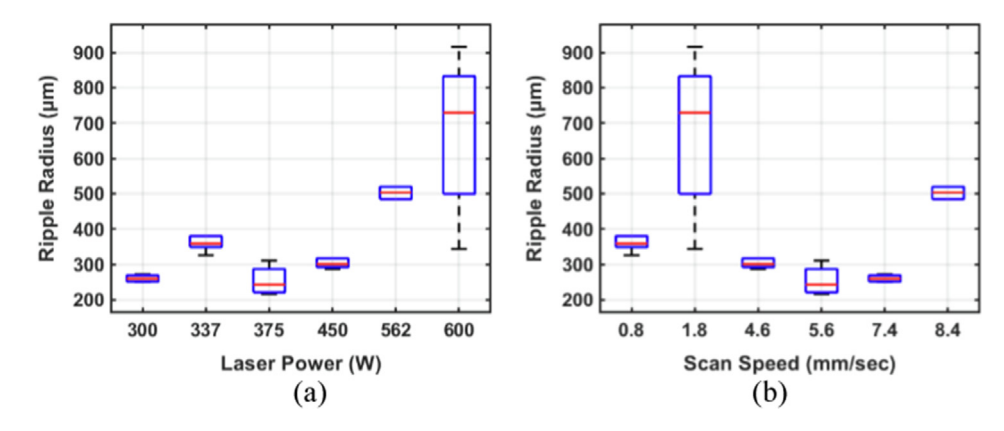


Fig. 4. A statistical description of the distribution of the ripple radius against different process settings; (a) variation of the ripple radius with laser power showing increases in ripple radius with the laser power; (b) variation in ripple radius with scan speed shows a decreasing trend in the ripple radius at high scan speed.

Table 3 Physical overlap calculated at three laser power settings to quantify the voids between consecutive scan tracks.

Ripple dia. (μm)	Hatch distance (μm)	Physical overlap (%)
520 (300 W)	528	-1.53
614 (450 W)	528	14
1320 (600 W)	528	60

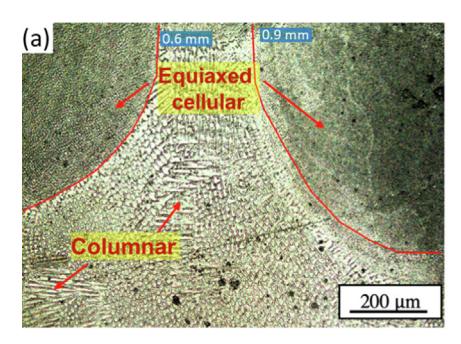
Observations at 200 μm Fig. 5 shows the representative optical micrographs obtained at 10x magnification. Here, the field of view was 2.65 mm. Fig. 5(a) was obtained from sample 4 that was printed at 600 W laser power and 1.80 mm/sec scan speed. Fig. 5 (b) was obtained from sample 5 that was printed at 450 W laser power, and 4.65 mm/sec scan speed. Fig. 5(c) was obtained from sample 9 that was printed at 300 W laser power and 7.40 mm/

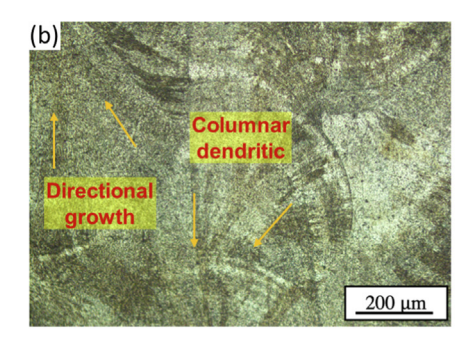
Table 4

Different segments classified from microstructure hierarchy and mapped in solidification map.

1	Center of ripple
1a	Cellular structure of size 50 μm^2 at center of ripple

- Cellular structure of size 100 µm² at center of ripple
- Segregated cellular structure
- Periphery of ripple
- Columnar dendritic structure between 0 and 20 μm from the periphery 2a of ripple
- 2b Elongated cellular structure between 20 and 50 μm from the periphery of ripple
- Edge of the scan track
- Columnar dendritic structure





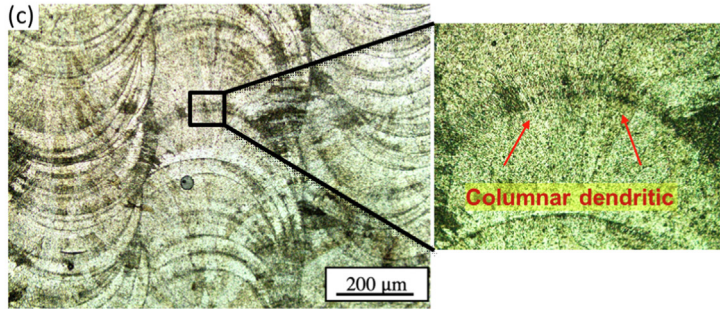


Fig. 5. Optical micrographs at 200 μm scale at three laser power settings: (a) 600 W showing columnar structure in the heat affected zone between two scan tracks and equiaxed structure inside the scan track; (b) 450 W showing directionality of columnar dendritic grains along the scan direction; (c) 300 W showing columnar dendritic at the periphery of a ripple.

sec scan speed.

The micrographs capture the spatial distribution of different microstructure clusters relative to the scan track boundary and the ripples. Fig. 5(a) is taken from the (heat-affected) zone adjoining two scan tracks. The structure is mostly composed of columnar dendrites with equiaxed grains present inside the scan track. At lower power settings and high scan speeds (Fig. 5(b, c)), the dendritic structure is not apparent as the grains tend to be highly refined.

The microstructure formations in a DED process can be explained in terms of the ratio of the local temperature gradient G (°C/mm) and solidification growth rate R (mm/s), i.e., the ratio G/R [19]. Due to a large distribution of thermal gradients in the melt pool, we are more likely to find heterogeneous microstructure as seen in Fig. 5(a) [20]. Evidently, the thermal gradients are the highest radially from the center to the edge of a ripple, as well as from the center to the edge of a scan track (i.e., along the width of the track). Consequently, the solid–liquid interface advances preferentially along the normal to the ripple boundaries and across the track. The resulting microstructure consists of equiaxed cellular grains in the interior of a ripple, and columnar dendritic structure oriented almost radially from the ripple boundary into the interior.

Observations at 100 \mu m Fig. 6 shows the representative micrographs at 20x magnification of a microscope field of view of 1.32 mm (at 100 μm length scale). Fig. 6(a) was obtained from sample 4 that was printed at 600 W laser power and 1.80 mm/sec scan speed. Fig. 6(b) was obtained from sample 5 that was printed at 450 W laser power, and 4.65 mm/sec. Fig. 6(c) was obtained from sample 9 that was printed at 300 W laser power and 7.40 mm/sec scan speed.

As shown in the figures, the spatial distribution of dendritic structures and their preferred orientations becomes more evident at this scale. For example, Fig. 6(a) is captured near the periphery of a ripple shown in Fig. 5(a). It reveals that at 600 W (high laser power) the microstructure consists of long columnar dendrite and cellular network structures with a sharp boundary separating these. The cellular structure exists in a few columnar grains

(marked in Fig. 6(a)) and has a cell length in the range of 0.06–0.1 mm. These cellular structure shows intragranular features which means the sub-grain structure (cellular structure) is constricted inside the large grains (columnar structure).

The sharp cooling rates prevailing in DED give rise to smaller-sized cells (seen at 50 μm scale length) compared to in a laser welding process [21]. These structures are spread over an average area of 270 μm^2 . At lower power settings, just as with 200 μm magnification microstructure, the dendritic structure is much finer and is not clearly visible at this magnification (see Fig. 6(b)). Nonetheless, the dendrites seem to have grown preferentially oriented radially inward or in the direction of a moving heat source (i.e., laser beam) from the periphery of ripples.

At a lower power setting of 300 W and high scan speeds (7.40 mm/sec), defects such as voids become apparent on the surface (see Fig. 6(c)). These voids occur due to the uneven melting of the powder, especially near the junction of scan tracks (consequence of the low energy input at the specified condition), coupled with the lack of sufficient material to compensate for the shrinkage (as a result of high scan speeds). Additionally, an equiaxed cellular structure is observed near the center of the ripple because of the high cooling rate of nearly $10^3 - 10^4$ K/s and moderately high solidification rates.

Observations at 50 \mu m Fig. 7 shows the representative micrographs at 50x magnification at microscope field of view of 0.53 mm (at 50 μm length scale). Fig. 7(a) was obtained from Sample 4 that was printed at 600 W laser power and 1.80 mm/sec scan speed. Fig. 7(b) was obtained from Sample 5 that was printed at 450 W laser power, and 4.65 mm/sec. Fig. 7(c) was obtained from Sample 9 that was printed at 300 W laser power and 7.40 mm/sec scan speed.

At this magnification, the micrographs show varied shades on a grey scale. Earlier studies suggested that the dark and light portions at this magnification are likely due to the differential etching among the various material species, especially the austenite (light) and ferrite (dark) phases obtained after solidification. Additionally, Fig. 7(a) shows a contrast between the cell core and boundary.

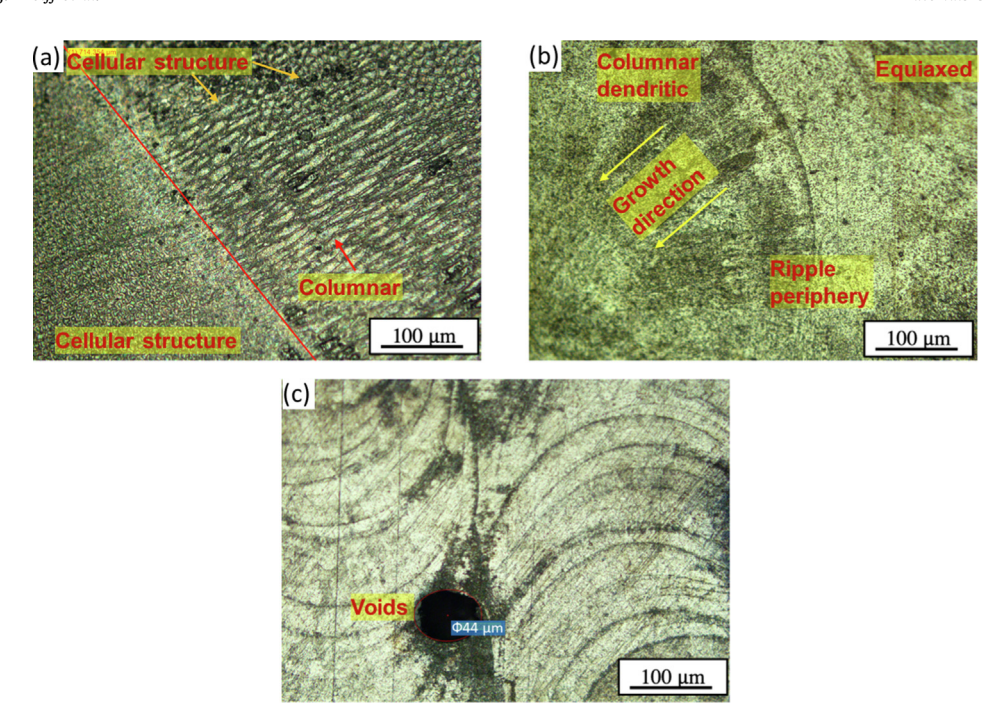


Fig. 6. Optical micrographs at 100 μm scale at three laser power settings: (a) 600 W showing a sharp boundary separating columnar and cellular structure near the periphery of ripple, and microsegregation pattern observed in the columnar dendritic zone; (b) 450 W showing columnar dendritic growth at the ripple periphery and edge of scan track whereas the equiaxed structure distributed outside the ripple periphery; (c) 300 W showing void formation between consecutive scan tracks due to negative overlap (-1.53%) at low laser power and high scan speed setting.

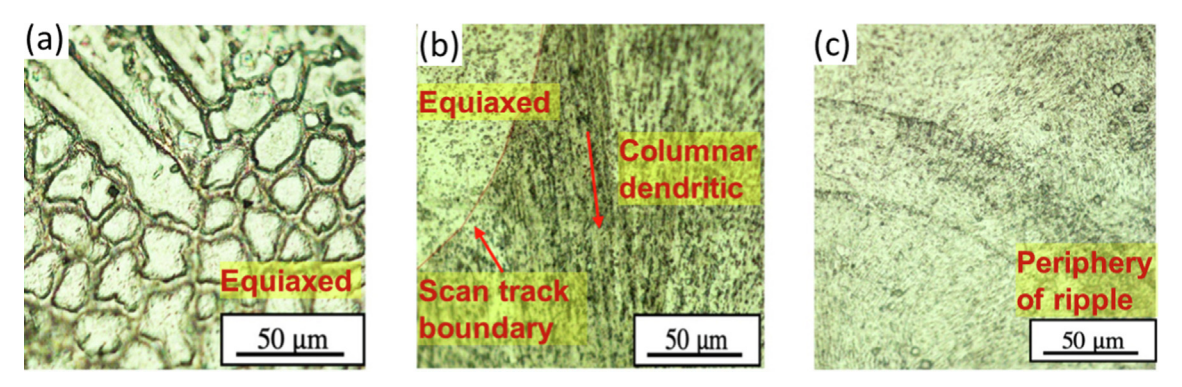


Fig. 7. Optical micrographs at $50 \, \mu m$ scale at three laser power settings: (a) $600 \, W$ showing the formation of cellular colonies at the center of a ripple; (b) $450 \, W$ shows a red-colored scan track boundary that distinguishes between columnar dendritic structure outside the track boundary and equiaxed structure inside the scan track; (c) $300 \, W$ showing columnar dendritic formations extending from the ripple periphery radially towards the center of a ripple. (For interpretation of the references to color in this figure legend, the reader is referred to the web version of this article.)

The etchant used here, agua regia, is known to preferentially attack the δ-ferrite and carbides such as Cr₂₃C₆ and Mo₂₃C₆ and thereby helps to identify the presence of the heavier elements at the cell boundary as seen in Fig. 8(a). As observed in the (Energy Dispersive Spectroscopy) EDS line scan in Fig. 8(b), Cr and Mo were found to be higher in mass percentage at the cell boundary than in the cell core. On the other hand, Ni concentrations were found to be higher in the cell core than at the cell boundary. An EDS spot analysis was performed at 6 different locations at the boundary and the interior. The Cr and Mo mass percentages at cell boundary, calculated from this analysis, were found to be 18.55% (standard deviation of 0.85%) and 4.45% (standard deviation of 0.64%), respectively, and 15.56% (standard deviation of 0.53%), and 3%, (standard deviation of 0.47%) respectively, at the cell core. This statistically significant depletion of Cr and Mo in the cell core is consistent with the earlier studies [22].

As a DED-printed 316L solidifies, austenite is the primary solid phase to emerge from the liquid melt pool. This is consistent with the earlier observations of austenite (γ -phase) forming at the core, and δ -ferrite between the dendrites as seen in Fig. 7(b) [23]. The dark portions in Fig. 7(b&c) are indicative of the dendrites containing δ -ferrite (which was revealed after the etching) forming near the scan track boundary. Also, fast-directional solidification and re-heating of a deposit formed along a scan track (owing to the subsequent deposition of material along adjacent scan tracks) can induce micro-segregation of γ and δ -phases within a dendrite.

4. Discussion

4.1. Heterogeneity of the DED dendritic structure

Fig. 9 summarizes the different microstructures, including the shape and the size of various formations at different positions on

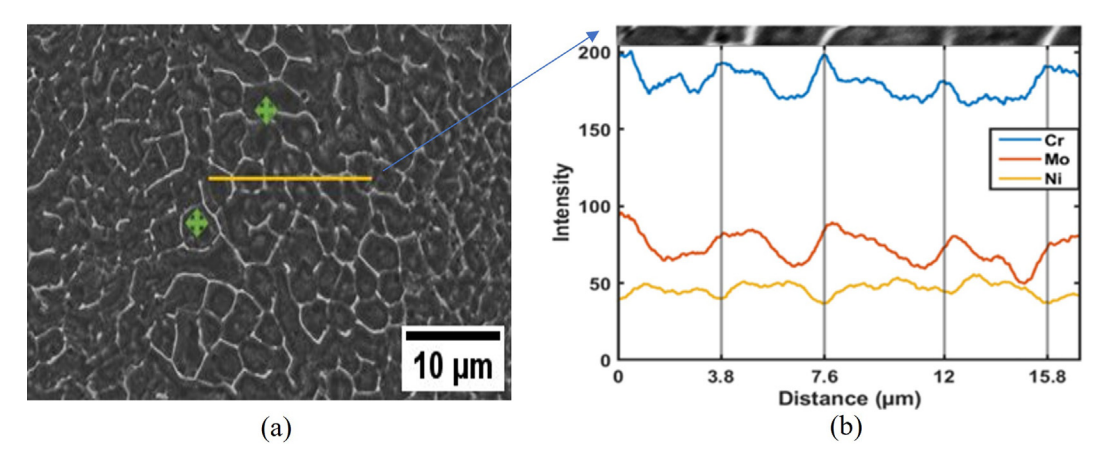


Fig. 8. A scanning electron microscopy (SEM) image showing equiaxed colonies on the surface of DED-printed 316L; (a) An Energy Dispersive Spectroscopy (EDS) analysis performed on two different spots to calculate the Cr and Mo mass percentages, one at cell boundary and another at cell core; (b) EDS line scan capturing Cr, Mo, and Ni variations suggests an increase in the concentration of Cr and Mo at the cell boundaries.

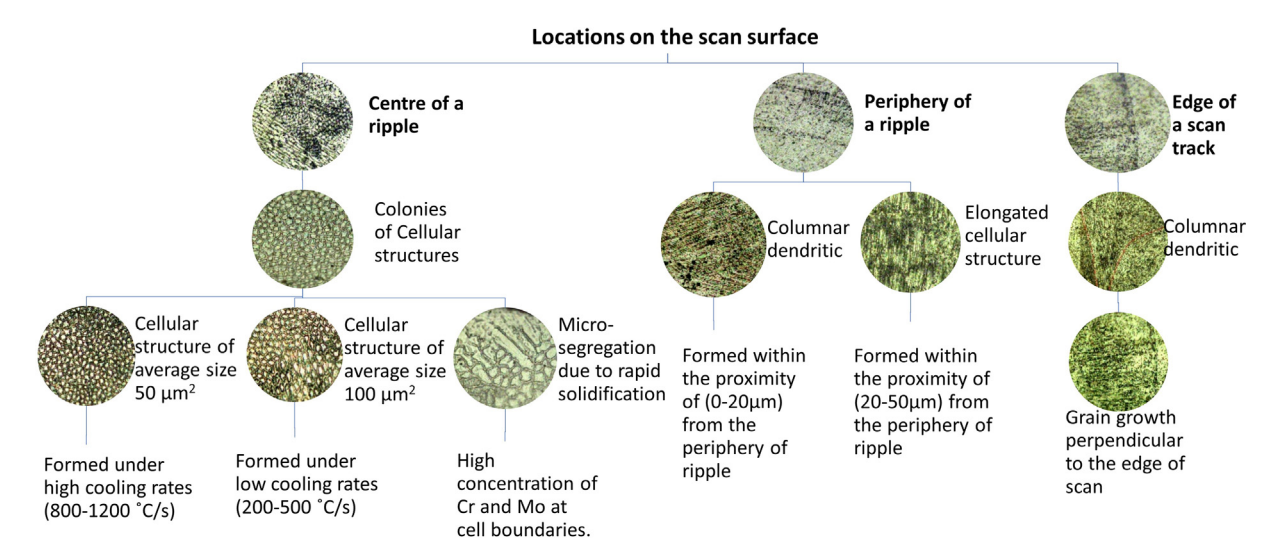


Fig. 9. The salient structures observed across various segments of the scan surface of a DED-printed 316L samples.

the sample surface, namely, the center of a ripple, the periphery of a ripple, and the edge of scan tracks as highlighted in Table 4. As noted earlier, the microstructure depends on the spatiotemporal distribution of the temperature gradient G (°C/mm) and solidification growth rate R (mm/s). While the ratio G/R, controls the solidification mode, the product $G \times R$ decides the size of grains [19]. Moving radially inward from the fusion line (or near the outer edge of ripple), the structure changes from equiaxed to columnar dendritic to cellular as shown earlier in Fig. 5(a). At a low laser power (300–450 W) and high scan speeds (4.65–8.46 mm/sec), a fine grain structure was observed (see Fig. 10). At high laser power (>450 W) and low scan speeds (0–4.65 mm/sec) a coarse dendritic structure was apparent. In addition to the size of structures, the laser power has a major effect on the formation of ripples (see Fig. 4).

4.2. Effect of laser power and scan speed on ripple geometry and scan track

The ripple formations, commonly observed in the welding processes, are attributed to five different phenomena, namely, thermocapillary force, power source variations, periodic swelling in the liquid metal, flow instability (recoil effect) due to evaporation,

and solidification dynamics [24]. Cheever *et al.* [8] observed the surface ripples on different thin metal sheets in gas tungsten arc, spot, and seam welding processes. They observed that sharp variations in the plasma pressure caused due to intermittent shut-off of the arc cause the oscillation of the weld pool during solidification and create ripples on the surface. Anthony and Cline [9] studied the surface ripples using laser surface melting techniques used for enhancing the surface property like transformation hardening of the surface. They inferred that the surface tension gradients were the main cause behind the surface ripples.

Wei et al. [10] studied the surface ripples in Electron Beam Welding of Al 1100 and SS304 specimens. They observed that the average amplitude and pitch of ripples increased with increasing dimensionless beam power, Marangoni, Prandtl, and Biot numbers and decreasing Stefan, and Peclet numbers. They studied the temperature dependence of surface tension (gradient of surface tension relative to temperature) in electron beam welding and noted that in low S concentration alloys, the surface tension gradient is negative leading to the formation of the shallow and wide melt pool, and positive in high S concentration alloys, leading to deep and narrow melt pools. They also observed that ripple roughness increases with the decreasing welding (scan) speeds. Based on these prior findings reported on the welding process, the ripple for-

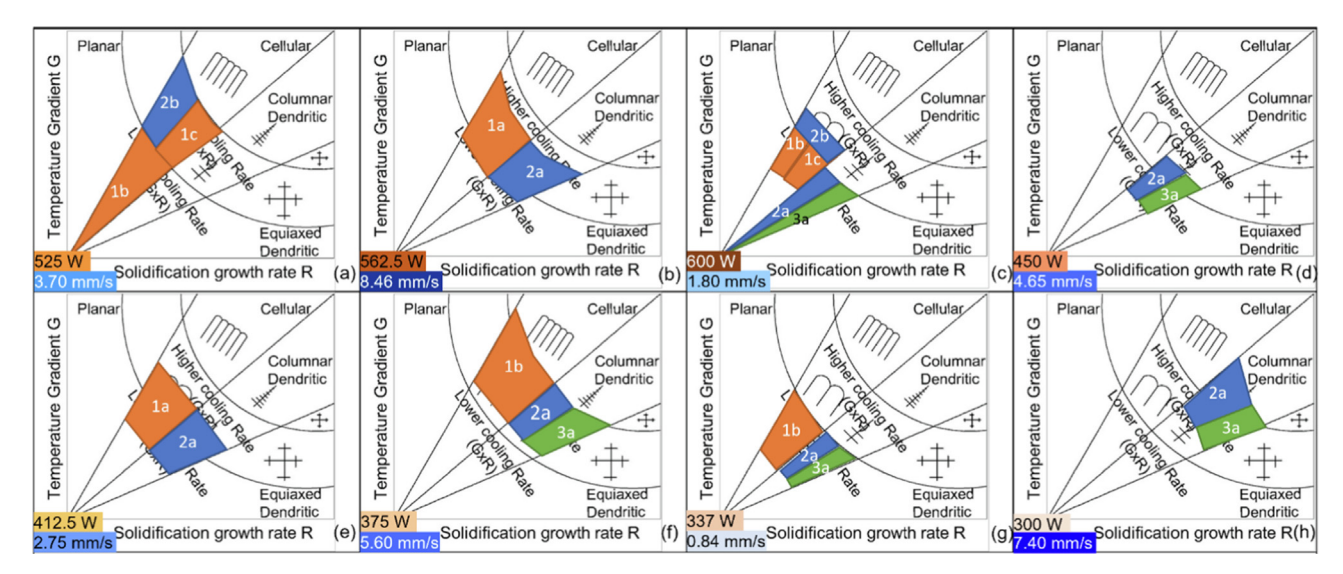


Fig. 10. The grain structures observed at different locations on the surfaces of the DED-printed 316L components mapped onto the Thermal gradient G vs. Solidification rate R plot.

mation in the DED process may be attributed to the following two phenomena.

- 1) Marangoni flow: The thermocapillary force or Marangoni flows takes place whenever a non-uniform temperature exists along with an interface. In DED, the surface directly beneath the Laser beam is hotter than the surface near the edges of the melt pool. This temperature difference induces the gradients in surface tension causing the liquid metal to move from the lower surface tension region to the higher surface tension region. For 316L surface tension increases when temperature decreases, i.e., the surface tension at the cooler edge of the pool will be higher than that at the centre. This creates a radially outward Marangoni flow that carries hot liquid to the edge of the pool, causing a shallow and wide melt pool as shown in Fig. 11. Marangoni flow can also be influenced by the amount of surface-active agents such as S and O present in the metal composition. A higher S content (>150 ppm) can alter the flow patterns to create a deep and narrow melt pool.
- 2) Recoil Pressure: During the melting process under the laser beam in DED, the particles move within the liquid metal with a certain kinetic energy. This kinetic energy increases with temperature and when these particles reach near the top surface of the melt pool, they have enough energy to escape the liquid metal into vapor. As shown in Fig. 12, vapor particles eject with momentum $(m_v v_v)$ from the liquid surface, causing the liquid to recoil with a momentum of (mv) where m is the mass of liquid surface and v is the velocity of the liquid surface. This exchange of momentum at the surface creates a recoil pressure which acts on the melt pool surface against the force induced by the vapours. It depresses the

molten layer downwards and disperses the liquid to the edges of the melt pool.

4.3. Amplitude and spacing of ripple

In a DED process for 316L, Marangoni (thermocapillary) flow patterns have the primary bearing on the melt pool flow patterns, especially near the solidification boundaries, and the recoil effect dominates the flow near the core of the melt pool. The observed ripple marks are largely informed by the Marangoni effect. According to Wei *et al.* [10] analytical model, the amplitude *a* of the ripples may be expressed as

$$a = (1 - K) \frac{\rho}{\gamma_m} \left[v \left(\left| \frac{d\gamma}{dT} \right| \frac{q_c h r_e}{k \mu} \right)^2 \right]^{\frac{2}{3}}$$

where K is the loss coefficient, ρ is the density, γ_m is the surface tension at melting temperature, v is the kinematic viscosity, μ is the dynamic viscosity, dT is the temperature difference between vertical walls, q_c is the incident flux, h is the fusion zone depth, r_e is the rear length of the melt pool, k is the liquid conductivity.

Wei *et al.* [10] also measured a experimentally using Kosaka surfcoder SE 3000 and analytically mapped the average amplitude to a working parameter p as

$$a = r \times p$$

where r is a proportionality constant determined for austenitic steels to be \sim 2.5, and it encapsulates the influence of the process

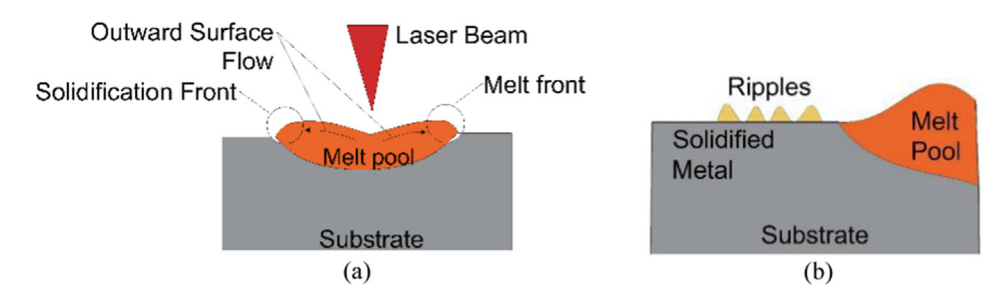


Fig. 11. An illustration of thermocapillary effect or Marangoni convection in the melt pool; (a) outward Marangoni flow due to negative temperature gradient of surface tensions causing a shallow and wide melt pool in 316L; (b) ripple formations containing multiple wavelengths and amplitude variations at the solidification front.

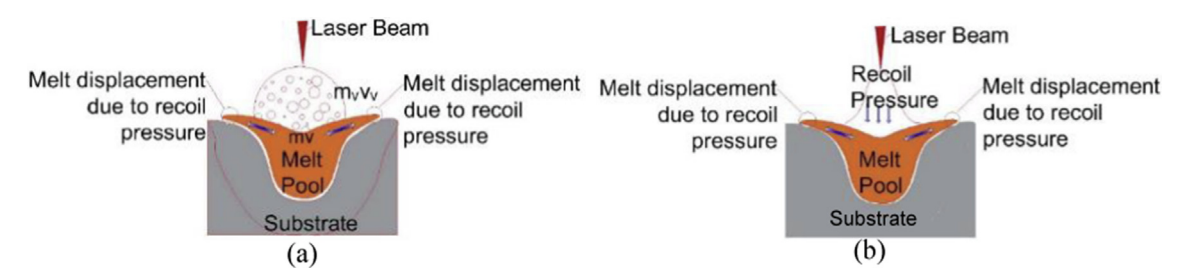


Fig. 12. An illustration of recoil pressure effect responsible for displacement of liquid melt in the melt pool; (a) exchange of momentum between vapor particles induces the recoil pressure; (b) displacement of liquid melt at the edge of melt pool due to the recoil pressure.

parameters and certain material properties on the thermocapillary flow. The working parameter *p* is given by

$$p \, = \, \left\{ [h_c(T_m - T_\infty) - \rho h_{sl} U]Qh^2 \right\}^{\frac{2}{3}} \times 10^{-4}$$

where, h_c = 25 Wm⁻²K⁻¹ is the heat transfer coefficient, $T_m - T_\infty = \Delta T$ c = 1000 K, ρ = 7040 kgm⁻³ is the density, h_{sl} = 250 Jkg⁻¹ is the latent heat for solidification, h = 0.3 \times 10⁻³ m is the fusion zone depth and for our case $U \in (0.00084 - 0.0084)$ ms⁻¹ is the scan speed, $Q \in (300 - 600)$ W is the laser power.

After substituting the values in the working parameter equation, we get $p = 0.77 \times 10^{-4}$ and the amplitude of ripples of 5 μ m. The value is consistent with the characteristic graph reported in the literature connecting the amplitude with the working parameter linearly [10]. It is evident from Eq. 3 that laser power and working parameter are directly proportional. As a result, the amplitude of the ripple increases as the laser power increases. Wei *et al.* [10] related the amplitude to the spacing (or the wavelength) s of surface ripples as

$$a = cs$$

where a is the amplitude of ripples, and c is a proportionality constant estimated empirically to be in the range of 0.015–0.03 for aluminum and steel alloys (e.g., Al 1100 and SS 304). The wavelength or spacing of the ripples calculated using Eq.4 range between 10^{-3} – 10^{-4} m, which is the same magnitude as that observed on the surface of steel alloys [10].

Our experimental results capturing the combined effect of laser power and scan speed on the ripple curvature, and ripple wavelength are summarized in Table 5. Here, the ripple curvature was determined as mentioned in Section 3. The wavelength of the ripple was estimated from the optical micrographs using the following procedure: Each micrograph was first converted to a grey scale image. The intensities values along five scan tracks, each of length $L = 2128~\mu m$ were selected and transformed obtain the corresponding frequency spectra. The frequency f with highest magnitude (e.g., see Fig. 13 (a, b)) was chosen from five Fourier spectrum. Next, the average ripple wavelength was calculated as $\lambda = \frac{L}{f}$, where λ is the salient ripple wavelength, L is the length of

Table 5Observations of surface morphology under different process parameters.

Process parameter		Observations		
Laser power	Scan speed (mm/	Ripple radius	Average wavelength (mm)	
(W)	sec)	(µm)		
562.5	8.46	514 (75)	1.34 (0.76)	
337	0.84	373 (37)	1.14 (0.88)	
300	7.40	260 (10)	0.50 (0.38)	
600	1.80	660 (230)	2.35 (0.80)	
450	4.65	307 (34)	1.81 (1.2)	
375	5.60	257 (34)	0.39 (0.21)	

the scan track and f is the frequency of where the magnitude is the highest. The amplitude of the ripple waveform for the salient (dominant) frequency band, as highlighted in Fig. 13(a,b), was estimated based on the mathematical expression (Eq. 3) provided in an earlier research work [10].

The average ripple wavelength of high energy density sample found to be 1.14 mm, with standard deviation of 0.80 mm whereas the average ripple wavelength of low energy density sample was 0.50 mm, with standard deviation of 0.51 mm. The plots of Fig. 13 (a, b) show frequency portraits obtained at high and low energy densities. In high energy density case, a sharp low frequency component predominated whereas in low energy density, a diffused high frequency component predominated which explains the effect of other factors beyond Marangoni convection influencing ripple geometry, which results in a small melt pool as the fluid in the melt pool becomes more stable.

Furthermore, the plot of Fig. 13 (c, d) illustrates the variation of the amplitudes with the frequency estimated using gaussian process regression which showed the low variability (standard deviation of 1.31×10^3) at low energy densities compared to high variability (standard deviation of 2.14×10^3) at high energy densities which provides us the evidence of complex periodic wave formation on the surface. When the laser power is low, and the scan speed is high (samples 7 & 9) the characteristic ripple wavelengths tend to be low due to the relatively short interaction time between the laser and the deposited material on the surface. In contrast, when the laser intensity is high and the scan speed is slow (sample 4), the interaction time and total energy transfer are high, leading to the increased ripple wavelengths. These experimental findings are consistent with the earlier findings in the welding literature (see [10] and Section 4.2) that an increase in the laser power and a decrease in the scan speed causes the ripple wavelength to

However, the ripple traces on the surface are much more complex and appear far from a single periodic wave representations employed in the literature. As shown in Table 5, low laser powers (300 W) produce ripples with smaller average spacing/wavelength of 0.508 mm (with a standard deviation of 0.38). In contrast, high laser powers (600 W) produce ripples with larger spacings with an average characteristic wavelength 2.351 mm (with a standard deviation of 0.80).

These variations in the ripple wavelengths suggest that additional phenomena beyond Marangoni convection, such as alloying effect, recoil pressure motion patterns, center purge argon gas pressure can be important determinants of the surface morphology. Pertinently, in-situ monitoring of the process employing high-speed cameras, melt pool cameras, and vibration/force sensors, may be necessary to directly observe the manifestation of these phenomena in creating surface ripples in a DED process.

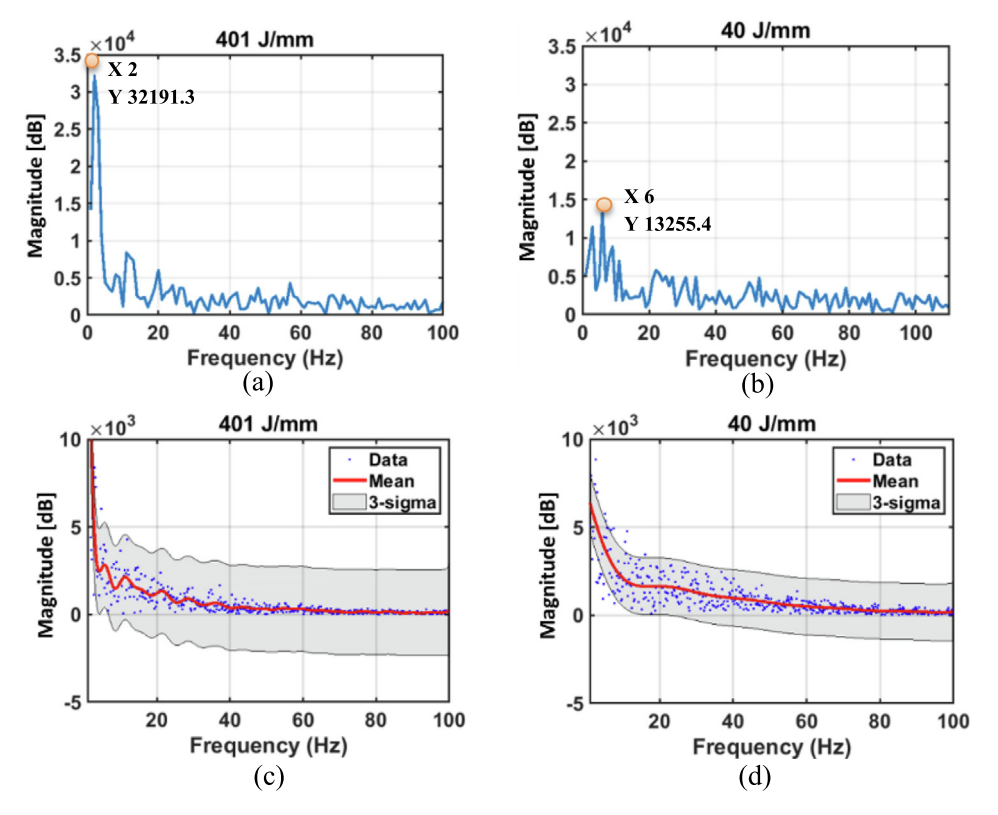


Fig. 13. Representative Fourier (amplitude) spectra of the ripple wave-like formations for (a) high energy density sample (Sample 8); (b) low energy density sample (Sample 9), and the corresponding amplitude variation of a (c) high energy density sample, and (d) low energy density sample suggesting an increase in the wavelength (and decreases in the dominant frequencies) of the ripple formations with increasing energy densities or laser power. Also, the wave formations exhibit considerable spatial variations (as captured in the 3-sigma band) indicating the limitation of the prior, largely rudimentary quantifications of the ripple geometry.

5. Conclusions

The present experimental study has investigated the surface morphology, especially the ripple pattern and microstructure of 316L printed in a DED process on an Optomec MTS 500 hybrid machine under different settings of the laser and scan speeds. The printed samples were polished to Ra < 30 nm, etched using Aqua Regia, and observed on an optical microscope at 4 different magnifications. Notably, only five earlier works focused on the microstructure of the surface of DED-printed 316L samples along the scan direction. The following are the key takeaways from this study.

- 1. While ripple formations have been studied in the context of welding processes and to extent in SLM, they have not received much attention in the DED literature. The micrographs at 500 μm scale capture certain distinct effects of the laser power and scan speed on the formation of ripples. It may be inferred that an increase of the laser power increases the ripple wavelength, and the ripple curvature. These observations are consistent with an earlier analytical model that predicts the spacing (wavelengths) of the ripples formed due to the thermocapillary effect.
- At 200 μm scale the formation of columnar/dendritic structures was evident and these formations were found to grow preferentially radially inward from ripple periphery and scan track boundary.
- 3. The influence of laser power is dominated in formation of voids and the microstructure development. In high laser power conditions, slow cooling rate allows more time for dendritic growth preferentially radially inward from the ripple periphery, as shown by the micrographs at 100 and 50 µm scale lengths. In

- contrast, at low laser power, the cooling rate is faster, resulting in fine dendritic structure. However due to reduced recoil pressure at low laser power, a negative overlap between consecutive scan tracks results in the formation of voids.
- 4. The cellular structure predominates at low scan speeds due to a moderate solidification growth rate caused by an increase in the laser-deposited material interaction time. As scan speed increases, the laser-deposited material interaction time decreases, this promotes rapid cooling and creates fine dendritic structure.
- 5. The present investigation also lays a foundation for future work on the closed-loop control of a DED process, especially of the resulting microstructure. It is pertinent to note that any real-time control input essentially influences and should be synthesized based on the prediction or measurement of the morphology, especially the ripple and scan track formations and the resulting microstructure of the scan surface. In this context, the machine tools implementing the DED process are increasingly being instrumented with a combination of in-situ sensors, such as the melt pool cameras, temperature sensors, and various vibration and acoustic emission (AE) sensors [14]. A closed-loop control of the process can be achieved by controlling the ripple structure based on fusing the information contained in these various in-situ measurements.
- 6. For several applications, the scan surface of a DED-printed part would be chosen as the load bearing and a contacting surface. Therefore, the microstructures and the morphological formations on the scan surface would influence the corrosion and wear resistance of the resulting component. The present study opens possibilities to perform a systematic analysis of beha-

viours and properties, such as corrosion resistance, hardness, wear resistance of the DED-printed component surfaces that bear the heterogeneous microstructure [53].

Data availability

Data will be made available on request.

Declaration of Competing Interest

The authors declare that they have no known competing financial interests or personal relationships that could have appeared to influence the work reported in this paper.

Acknowledgement

The author would like to acknowledge the support from the Texas A&M University XGrants and National Science Foundation (S&AS grant award #1849085 and ECCS 1953694) for their generous support.

Appendix A. Supplementary data

Supplementary data to this article can be found online at https://doi.org/10.1016/j.matdes.2023.111756.

References

- L. Team, DED and Large-Format Additive Manufacturing Markets: 2021-2030, SmarTech Analysis. https://www.smartechanalysis.com/reports/ded-and-large-format-additive-manufacturing-markets-2021-2030/ (accessed Oct. 24, 2022).
- [2] R. Liu, Z. Wang, T. Sparks, F. Liou, J. Newkirk, 13 Aerospace applications of laser additive manufacturing, Elsevier Ltd (2017), https://doi.org/10.1016/ B978-0-08-100433-3.00013-0.
- [3] H. Liu, Z. Hu, X. Qin, Y. Wang, J. Zhang, S. Huang, Parameter optimization and experimental study of the sprocket repairing using laser cladding, Int. J. Adv. Manuf. Technol. 91 (9–12) (2017) 3967–3975, https://doi.org/10.1007/ s00170-017-0066-y.
- [4] M.L. Griffith, L.D. Harwell, J. Romero, E. Schlienger, C.L. Atwood, J.E. Smugeresky, Multi-material processing by LENS, Solid Free. Fabr. Symp. (1997) 387–393.
- [5] A. Yadollahi, D. Seely, B. Patton, N. Shamsaei, and S. M. Thompson, Mechanical and microstructural properties of LENS-produced AISI 316I stainless steel, 56th AIAAASCEAHSASC Struct. Struct. Dyn. Mater. Conf., no. January, pp. 1–8, 2015.
- [6] M. Godec, S. Zaefferer, B. Podgornik, M. Šinko, E. Tchernychova, Quantitative Multiscale Correlative Microstructure Analysis of Additive Manufacturing of Stainless Steel 316L Processed by Selective Laser Melting, Mater. Charact. (2019), https://doi.org/10.1016/j.matchar.2019.110074 110074.
- [7] S.F. Yang, C.W. Li, A.Y. Chen, B. Gan, J.F. Gu, Microstructure and corrosion resistance of stainless steel manufactured by laser melting deposition, J. Manuf. Process. 65 (March) (2021) 418–427, https://doi.org/10.1016/j. jmapro.2021.03.051.
- [8] D.L. Cheever, Mechanism of Ripple Formation During Weld Solidification.
- [9] T.R. Anthony, H.E. Cline, Surface rippling induced by surface-tension gradients during laser surface melting and alloying, J. Appl. Phys. 48 (9) (1977) 3888– 3894, https://doi.org/10.1063/1.324260.
- [10] P.S. Wei, C.Y. Chang, C.T. Chen, Surface Ripple in Electron-Beam Welding Solidification, J. Heat Transf., vol. 118, no. November, 1996.
- [11] N. Senin, A. Thompson, R.K. Leach, Characterisation of the topography of metal additive surface features with different measurement technologies, Meas. Sci. Technol., vol. 28, no. 9, 2017, 10.1088/1361-6501/aa7ce2.
- [12] N. Senin, A. Thompson, R. Leach, Feature-based characterisation of signature topography in laser powder bed fusion of metals, Meas. Sci. Technol., vol. 29, no. 4, 2018, 10.1088/1361-6501/aa9e19.
- [13] P. Tang et al., The Formation of Humps and Ripples During Selective Laser Melting of 316l Stainless Steel, JOM 72 (3) (Mar. 2020) 1128–1137, https://doi. org/10.1007/s11837-019-03987-7.
- [14] A.S. Iquebal, B. Botcha, S. Bukkapatnam, Towards rapid, in situ characterization for materials-on-demand manufacturing, Manuf. Lett. 23 (2020) 29–33, https://doi.org/10.1016/j.mfglet.2019.11.002.
- [15] M. Liu, A. Kumar, S. Bukkapatnam, M. Kuttolamadom, A Review of the Anomalies in Directed Energy Deposition (DED) Processes & Potential Solutions - Part Quality & Defects, Procedia Manuf. 53 (2021) 507–518, https://doi.org/10.1016/j.promfg.2021.06.093.

- [16] C. Zhong, Experimental study of effects of main process parameters on porosity, track geometry, deposition rate, and powder efficiency for high deposition rate laser metal deposition, vol. 042003, 2015, 10.2351/1.4923335.
- [17] J. Hu, H. Guo, H. L. Tsai, Weld pool dynamics and the formation of ripples in 3D gas metal arc welding, vol. 51, pp. 2537–2552, 2008, 10.1016/j. ijheatmasstransfer.2007.07.042.
- [18] J. Mazumder, J. Choi, K. Nagarathnam, J. Koch, D. Hetzner, The direct metal deposition of H13 tool steel for 3-D components, Jom 49 (5) (1997) 55–60, https://doi.org/10.1007/BF02914687.
- [19] J.D. Hunt, Steady State Columnar and Equiaxed Growth of Dendrites and Eutectic, Mater. Sci. Eng. 65 (1984) 75–83.
- [20] F. Weng, S. Gao, J. Jiang, J.J. Wang, P. Guo, A novel strategy to fabricate thin 316L stainless steel rods by continuous directed energy deposition in Z direction, Addit. Manuf. 27 (March) (2019) 474–481, https://doi.org/10.1016/j. addma.2019.03.024.
- [21] Y. Zhong, L. Liu, S. Wikman, D. Cui, Z. Shen, Intragranular cellular segregation network structure strengthening 316L stainless steel prepared by selective laser melting, J. Nucl. Mater. 470 (2016) 170–178, https://doi.org/10.1016/j. jnucmat.2015.12.034.
- [22] G.F. Vander Voort, G.M. Lucas, E.P. Manilova, Metallography and Microstructures of Stainless Steels and Maraging Steels, Metallogr. Microstruct., vol. 9, no. c, pp. 670–700, 2018, 10.31399/asm.hb.v09.a0003767.
- [23] N. Suutala, T. Takalo, Austenitic Stainless Steel Welds, vol. l, no. May, pp. 717–725, 1980.
- [24] P.S. Wei, Thermal Science of Weld Bead Defects: A Review, J. Heat Transf. 133 (March) (2011) 2011, https://doi.org/10.1115/1.4002445.
- [25] J.D. Majumdar, A. Pinkerton, Z. Liu, I. Manna, L. Li, Microstructure characterisation and process optimization of laser assisted rapid fabrication of 316L stainless steel, Appl. Surf. Sci. 247 (2005) 320–327, https://doi.org/ 10.1016/j.apsusc.2005.01.039.
- [26] K. Zhang, S. Wang, W. Liu, X. Shang, Characterization of stainless steel parts by Laser Metal Deposition Shaping, Mater. Des. 55 (2014) 104–119, https://doi. org/10.1016/j.matdes.2013.09.006.
- [27] M.H. Farshidianfar, A. Khajepour, A.P. Gerlich, Effect of real-time cooling rate on microstructure in Laser Additive Manufacturing, J. Mater. Process. Technol. 231 (2016) 468–478, https://doi.org/10.1016/j.jmatprotec.2016.01.017.
- [28] Y. Yang, Y. Gong, C. Li, X. Wen, J. Sun, Mechanical performance of 316 L stainless steel by hybrid directed energy deposition and thermal milling process, J. Mater. Process. Technol., vol. 291, no. December 2020, p. 117023, 2021, 10.1016/j.jmatprotec.2020.117023.
- [29] O. Freneaux, J.B. Poulet, O. Lepre, G. Montavon, Coaxial nozzle for surface treatment by laser irradiation, with supply of materials in powder form, Google Patents (1995).
- [30] D. Boisselier, S. Sankaré, Influence of Powder Characteristics in Laser Direct Metal Deposition of SS316L for Metallic Parts Manufacturing, Phys. Procedia 39 (2012) 455–463, https://doi.org/10.1016/j.phpro.2012.10.061.
- [31] K. Mahmood, A.J. Pinkerton, Direct laser deposition with different types of 316L steel particle: A comparative study of final part properties, Eng. Manuf. 227 (4) (2013) 520–531, https://doi.org/10.1177/0954405413475961.
- [32] S. Wang, S. Zhang, C.H. Zhang, C.L. Wu, J. Chen, M.B. Shahzad, Effect of Cr 3 C 2 content on 316L stainless steel fabricated by laser melting deposition, Vacuum 147 (2018) 92–98, https://doi.org/10.1016/j.vacuum.2017.10.027.
- [33] X. Wang, D. Deng, M. Qi, H. Zhang, Influences of deposition strategies and oblique angle on properties of AISI316L stainless steel oblique thin-walled part by direct laser fabrication, Opt. Laser Technol. 80 (2016) 138–144, https://doi. org/10.1016/j.optlastec.2016.01.002.
- [34] P. Guo, B. Zou, C. Huang, H. Gao, Study on microstructure, mechanical properties and machinability of efficiently additive manufactured AISI 316L stainless steel by high-power direct laser deposition, J. Mater. Process. Technol. 240 (2017) 12–22. https://doi.org/10.1016/j.imatprotec.2016.09.005.
- Technol. 240 (2017) 12–22, https://doi.org/10.1016/j.jmatprotec.2016.09.005.

 [35] M. Mukherjee, Effect of build geometry and orientation on microstructure and properties of additively manufactured 316L stainless steel by laser metal deposition, Materialia 7 (May) (2019) 5–8, https://doi.org/10.1016/j.mtla.2019.100359.
- [36] F. Khodabakhshi, M.H. Farshidianfar, A.P. Gerlich, M. Nosko, V. Trembo, A. Khajepour, Effects of laser additive manufacturing on microstructure and crystallographic texture of austenitic and martensitic stainless steels, Addit. Manuf. 31 (June) (2019) 2020. https://doi.org/10.1016/j.addma.2019.100915.
- Manuf. 31 (June) (2019) 2020, https://doi.org/10.1016/j.addma.2019.100915.

 [37] Y. Balit, C. Guévenoux, A. Tanguy, M.V. Upadhyay, E. Charkaluk, A. Constantinescu, High resolution digital image correlation for microstructural strain analysis of a stainless steel repaired by Directed Energy Deposition, Mater. Lett. 270 (2020), https://doi.org/10.1016/j.matlet.2020.127632 127632.
- [38] Y. Balit, L. Joly, F. Szmytka, S. Durbecq, E. Charkaluk, A. Constantinescu, Selfheating behavior during cyclic loadings of 316L stainless steel specimens manufactured or repaired by Directed Energy Deposition, Mater. Sci. Eng. A, vol. 786, no. October 2019, p. 139476, 2020, 10.1016/j.msea.2020.139476.
- [39] E. Tan Zhi'En, J.H.L. Pang, J. Kaminski, Directed energy deposition build process control effects on microstructure and tensile failure behaviour, J. Mater. Process. Technol., vol. 294, no. November 2020, p. 117139, 2021, 10.1016/j. jmatprotec.2021.117139.
- [40] M. Ma, Z. Wang, X. Zeng, A comparison on metallurgical behaviors of 316L stainless steel by selective laser melting and laser cladding deposition, Mater. Sci. Eng. A 685 (2017) 265–273, https://doi.org/10.1016/j.msea.2016.12.112.
 [41] A. Saboori et al., An investigation on the effect of powder recycling on the
- [41] A. Saboori et al., An investigation on the effect of powder recycling on the microstructure and mechanical properties of AISI 316L produced by Directed

- Energy Deposition, Mater. Sci. Eng. A 766 (August) (2019) 138360, https://doi.org/10.1016/j.msea.2019.138360.
- [42] J. Wang, Effect of External Magnetic Field on the Microstructure of 316L Stainless Steel Fabricated by Directed Energy Deposition, Int. Mech. Eng. Congr. Expo. (2019) 1–5.
- [43] B. Zheng et al., On the evolution of microstructure and defect control in 316L SS components fabricated via directed energy deposition, Mater. Sci. Eng. A 764 (July) (2019) 138243, https://doi.org/10.1016/j.msea.2019.138243.
- [44] Y. Huang, M. Ansari, H. Asgari, M. Hossein, Rapid prediction of real-time thermal characteristics, solidi fi cation parameters and microstructure in laser directed energy deposition (powder- fed additive manufacturing), J. Mater. Process. Tech 274 (February) (2019) 116286, https://doi.org/10.1016/j. jmatprotec.2019.116286.
- [45] B. Rankouhi, K.M. Bertsch, G.M. De Bellefon, M. Thevamaran, D.J. Thoma, and K. Suresh, Experimental validation and microstructure characterization of topology optimized, additively manufactured SS316L components, Mater. Sci. Eng. A, vol. 776, no. August 2019, p. 139050, 2020, 10.1016/j. msea.2020.139050.
- [46] J.C. Haley, J.M. Schoenung, E.J. Lavernia, Modelling particle impact on the melt pool and wettability effects in laser directed energy deposition additive manufacturing, Mater. Sci. Eng. A 761 (June) (2019) 138052, https://doi.org/ 10.1016/j.msea.2019.138052.

- [47] A. Aggarwal et al., Role of impinging powder particles on melt pool hydrodynamics, thermal behaviour and microstructure in laser-assisted DED process: A particle-scale DEM – CFD – CA approach, Int. J. Heat Mass Transf. 158 (2020) 119989, https://doi.org/10.1016/j.ijheatmasstransfer.2020.119989.
- [48] A.C. Hall, C.V. Robino, Association of microstructural features and rippling phenomenon in 304 stainless steel gas tungsten arc welds, Sci. Technol. Weld. Join. 9 (2) (Apr. 2004) 103–108, https://doi.org/10.1179/ 136217104225017008.
- [49] J. Shao, G. Yu, X. He, S. Li, Z. Li, X. Wang, Process maps and optimal processing windows based on three-dimensional morphological characteristics in laser directed energy deposition of Ni-based alloy, Opt. Laser Technol. 142 (Oct. 2021), https://doi.org/10.1016/j.optlastec.2021.107162 107162.
- [50] T. Yang et al., The influence of process parameters on vertical surface roughness of the AlSi10Mg parts fabricated by selective laser melting, J. Mater. Process. Technol. 266 (Apr. 2019) 26–36, https://doi.org/10.1016/j. jmatprotec.2018.10.015.
- [51] R. Hu et al., Selective Laser Melting under Variable Ambient Pressure: A Mesoscopic Model and Transport Phenomena, Engineering 7 (8) (Aug. 2021) 1157–1164, https://doi.org/10.1016/j.eng.2021.07.003.
- [52] Botcha, Bhaskar, Ashif S. Iquebal, and Satish TS Bukkapatnam. "Smart manufacturing multiplex." *Manufacturing Letters* 25 (2020): 102-106.
- [53] Satish TS. Bukkapatnam, Autonomous materials discovery and manufacturing (AMDM): A review and perspectives, IISE Transactions 55 (1) (2023) 75–93.